

Aluminum Nanocrystals

Michael J. McClain,^{†,#} Andrea E. Schlather,^{†,#} Emilie Ringe,^{†,‡,#} Nicholas S. King,^{§,#} Lifei Liu,^{§,#} Alejandro Manjavacas,^{§,#} Mark W. Knight,^{||,#} Ish Kumar,[†] Kenton H. Whitmire,[†] Henry O. Everitt,[∇] Peter Nordlander,^{§,||,#} and Naomi J. Halas^{*,†,‡,§,||,⊥,#}

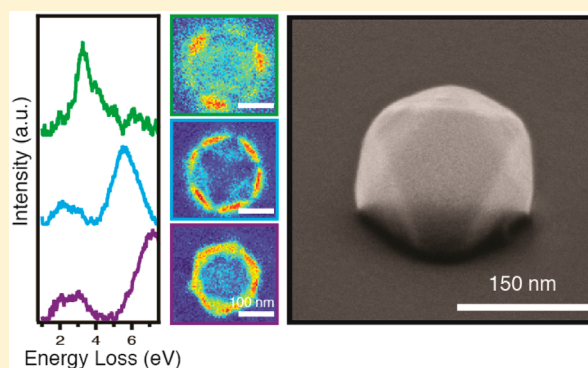
[†]Department of Chemistry, [‡]Department of Materials Science and Nanoengineering, [§]Department of Physics and Astronomy, ^{||}Department of Electrical and Computer Engineering, [⊥]Department of Bioengineering, and [#]Laboratory for Nanophotonics, Rice University, Houston, Texas 77005, United States

[∇]Army Aviation and Missile RD&E Center, Redstone Arsenal, Alabama 35898, United States

Supporting Information

ABSTRACT: We demonstrate the facile synthesis of high purity aluminum nanocrystals over a range of controlled sizes from 70 to 220 nm diameter with size control achieved through a simple modification of solvent ratios in the reaction solution. The monodisperse, icosahedral, and trigonal bipyramidal nanocrystals are air-stable for weeks, due to the formation of a 2–4 nm thick passivating oxide layer on their surfaces. We show that the nanocrystals support size-dependent ultraviolet and visible plasmon modes, providing a far more sustainable alternative to gold and silver nanoparticles currently in widespread use.

KEYWORDS: Plasmon, UV, aluminum, nanocrystal, synthesis



Noble metal nanoparticles are used extensively for applications such as photocatalysis or biological and chemical sensing.^{1–8} Interest in these nanoparticles has been based largely on their vivid optical properties, which are due to their collective electronic resonances, known as localized surface plasmons. Exquisite size and shape control has been achieved in the synthesis of noble metal nanoparticles such as gold, silver, and platinum, but the intrinsic properties and high cost of these noble metals present significant limitations for large-scale use.^{7,9,10} Gold nanoparticles have been of interest in applications involving visible and near-infrared light, and while the plasmon resonance of silver can also be excited at wavelengths that extend into the ultraviolet region of the spectrum, its conversion from silver to silver oxide limits its long-term stability. The UV region ($\lambda = 100\text{--}400\text{ nm}$) is of great interest in numerous applications; for example, most organic molecules have a strong absorption in the ultraviolet, allowing for ultrasensitive chemical sensing. Short wave UV light ($\lambda < 280\text{ nm}$) is capable of breaking organic bonds, which is key to sterilization, remediation, and photocatalysis applications.

Aluminum is the most abundant metal in the earth's crust and can support a UV plasmon resonance.^{3–5,7} Recent research on lithographically fabricated aluminum nanostructures demonstrated that the plasmon resonance is highly sensitive to oxygen content, redshifting and attenuating the plasmon resonance with increasing oxygen content.^{4,11} Chemical methods for the synthesis of Al nanoparticles have involved

the thermal decomposition of an aluminum hydride with a titanium catalyst but size and shape control have proven to be problematic with this approach.^{12–20} In this Letter, we report the facile synthesis of highly regular, faceted aluminum nanocrystals with controllable nanocrystal diameters ranging from 70 to greater than 200 nm. The optical properties of individual Al nanocrystals were measured using dark-field spectroscopy, cathodoluminescence (CL), and electron-energy loss spectroscopy (EELS), which clearly show the size-dependent, continuous tuning of the optical resonance from ultraviolet to the visible region of the spectrum with increasing nanocrystal diameter. The Al nanocrystals are terminated with a self-limiting, 2–4 nm oxide layer, which imparts stability, an important property that can ultimately enable their use in many different types of applications.

The aluminum nanocrystals were synthesized by adding a capping agent to the reaction shown in Figure 1a. The nanocrystals shown were synthesized using Schlenk line and glovebox techniques. All solvents and reagents were purchased from Sigma-Aldrich and dried and distilled under inert atmosphere before use. Tetrahydrofuran (THF) and 1,4-dioxane were added to a dry Schlenk flask under Ar atmosphere. Varying volume fractions of THF and 1,4-dioxane

Received: February 12, 2015

Revised: March 9, 2015

Published: March 19, 2015

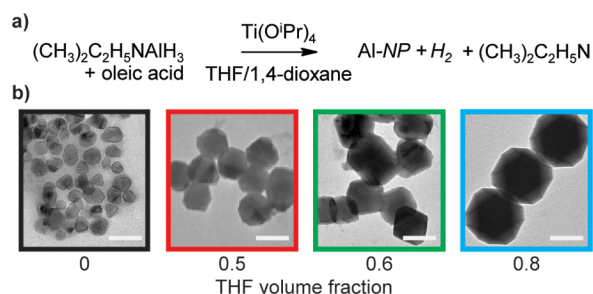


Figure 1. Size control of aluminum nanocrystals. Increasing the fraction of THF in the 1,4-dioxane/THF solution yields larger nanocrystals. (a) Reaction scheme for synthesis of aluminum nanocrystals. (b) Representative TEM images from synthesis with 0, 0.5, 0.6, and 0.8 THF volume fractions in a THF/1,4-dioxane solution (from left to right) (scale bar = 100 nm).

were added to equal 25 mL of solvent. The flask was heated in a 40 °C oil bath. The reaction takes more than 12 h to complete at room temperature and less than half an hour at 70 °C. Although they required 2 h for the reaction to complete, particles made at 40 °C showed better size distributions than those obtained at the higher reaction temperature of 70 °C. While the solvent was stirring, 6.5 mL of 0.5 M *N,N*-dimethylethylamine alane was added. A 0.5 mL sample of a 3.3 mM solution of titanium(IV) isopropoxide in toluene was added rapidly via syringe. The role of titanium is not explicitly clear, however, a variety of plausible mechanisms in similar types of reactions have been proposed.^{15,21} After 2.5 min, 0.5 mL of a 250 mM solution of oleic acid in 1,4-dioxane was added rapidly via syringe and the solution turned from clear to brown. The reaction proceeded for 2 h during which the reaction turned from black to gray: the smaller the resulting particles, the darker the solution. The reaction was removed from the heat source and stirred at room temperature for 1 h. Vacuum was applied to the solution to remove dimethylethylamine. The particles were then cleaned with centrifugation and sonication in dry THF to remove any unreacted alane, followed by three cycles in isopropanol. Isopropanol helps separate the particles from the capping agent. An oxide layer forms in this process that allows the particles to be stable for weeks (Supporting Information Figure S1). The particles were analyzed with X-ray photoelectron spectroscopy to confirm they are aluminum, and XPS-depth profiling demonstrates the particles are covered with an aluminum oxide layer (Supporting Information Figure S2).

The ratio of THF and dioxane is vital in controlling the sizes of the aluminum nanocrystals obtained by this approach, however their precise role is elusive. We did not observe size or shape control when we varied capping agent concentration, which was also observed in organic phase synthesis of indium nanocrystals.²² When toluene was substituted for dioxane (toluene has a similar viscosity to THF but a dielectric constant similar to dioxane) the resulting particles had the same size and shape as with the same ratio of THF/dioxane. These results suggest that particle size is more directly related to the dielectric properties of the solution and not to its viscosity.

Histograms of the particles presented in Figure 1 were generated by measuring the sizes of 200 particles from each reaction of a given volume fraction (Supporting Information Figure S3). The average sizes corresponding to each volume fraction from Figure 1b (left to right) are, with the associated standard deviations, 55 ± 11 , 117 ± 11 , 152 ± 35 , and $223 \pm$

32 nm. Several shapes are present and we observed no change in the percentage of each shape for particles made with different fractions of THF. There are approximately 30% truncated trigonal bipyramids, 30% octahedra, 10% icosahedra, and the remaining 30% are mixed irregular crystals.

The optical properties of individual nanocrystals were obtained using a custom-built UV–visible dark-field microscope (Figure 2). For the dark-field measurements, a solution

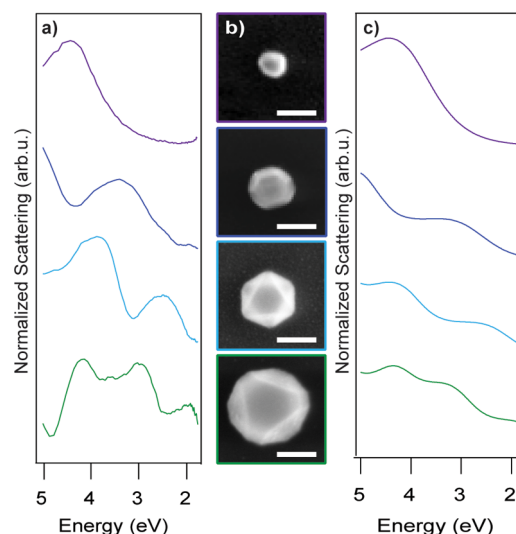


Figure 2. Dark-field spectroscopy of single aluminum nanocrystals. (a) Experimental dark field spectra of 80, 120, 155, and 220 nm nanocrystals (top to bottom) (Scale bar = 100 nm). (b) SEM images of respective particles. (c) Theoretical calculation of spectra obtained using Mie theory, assuming spherical nanoparticles coated with a 3 nm oxide layer in a homogeneous dielectric environment.

of aluminum nanocrystals was spin-coated onto a quartz substrate, and a scanning electron microscope (SEM) image of each nanocrystal was obtained following the measurement of its optical properties. The scattering spectrum of a series of nanocrystals of increasing size is shown in Figure 2a. In each case, the spectrum is dominated by the dipolar plasmon mode of the nanocrystal, which redshifts with increasing nanocrystal diameter. For nanocrystal sizes of 120 and 150 nm, we also observe a higher energy quadrupole mode at 5 and 4 eV, respectively. In this size range, the nanocrystal diameter is nearly half the size of the plasmon resonant wavelength, which results in significant optical phase retardation, increasing the magnitude of the higher order modes observed in the scattering spectrum. The SEM images in Figure 2b are particles corresponding to each spectrum in Figure 2a. A compilation of the dipolar and quadrupolar mode energies obtained from dark field scattering measurements of more individual nanocrystals is in Supporting Information Figure S4. Ensemble measurements do not retain the clear spectral response and we attribute this observation to the strong dependence of the plasmon resonance on nanocrystal size, not the shape polydispersity, which is not significantly large.

The experimental dark-field spectra were compared with theoretical calculations obtained using Mie theory for similarly sized particles.²³ Specifically, we model the aluminum nanoparticles as spheres coated by a 3 nm oxide layer with a diameter chosen to match the volume of the experimentally synthesized nanocrystals. As shown in Supporting Information Figure S5, this approach produces scattering spectra that agree

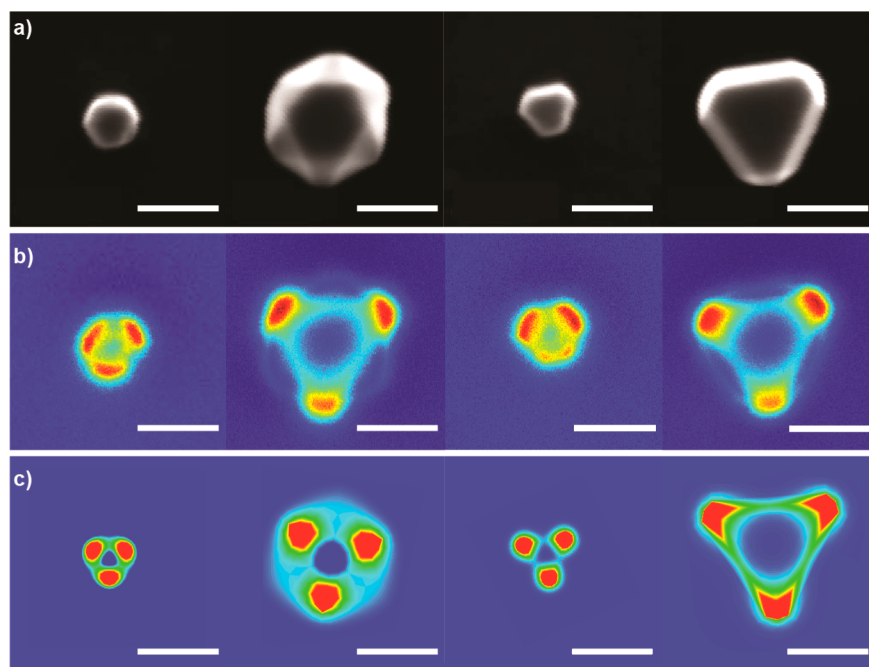


Figure 3. Cathodoluminescence images of the smallest and largest particles reveal similar charge density plots for varying sizes and shapes. (a) SEM images of 70 and 155 nm icosahedra and 65 and 155 nm truncated trigonal bipyramids (right to left). (b) Cathodoluminescence reveals a 3-fold symmetry mode between 1.77 and 3.54 eV. (c) Calculated cathodoluminescence images simulated using a single dipole excitation. Scale bar = 100 nm.

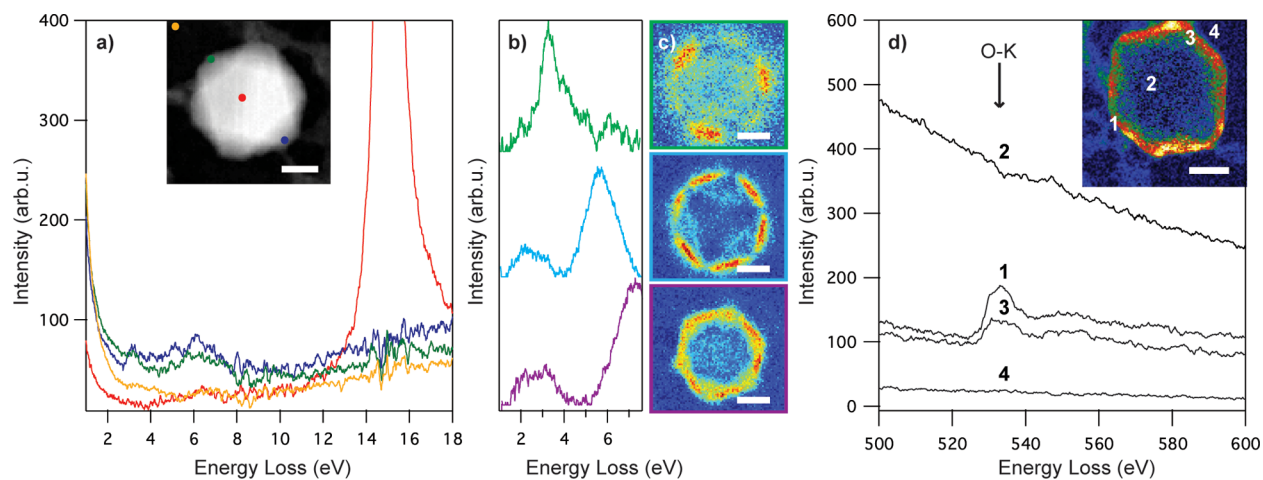


Figure 4. Electron microscopy and spectroscopy of Al nanocrystals. (a) Raw, low-loss, LSPR, and Al bulk plasmon data of a 166 nm particle from the positions shown in the inset. (b) EELS spectral components extracted by non-negative matrix factorization for the particle in (a). (c) EELS maps representing the spatial distribution of the LSPR corresponding to the spectra in (b). (d) Core-loss EELS of a 166 nm Al nanocrystal at multiple positions showing the O–K peak (indicated by the arrow) and (inset) background-subtracted O–K intensity map. Scale bars = 50 nm.

well with those obtained from a fully numerical simulation of Maxwell's equations for the experimental geometry. Furthermore, we approximate the effect of the dielectric substrate by assuming a homogeneous environment with an effective dielectric function equal to the average of the vacuum and substrate dielectric functions. Using the same illumination and collection conditions as in the experiment, we obtain theoretical spectra that agree remarkably well with the experimental measurements. Agreement between theory and experiment is best for smaller nanocrystal sizes; as their size increases, departure from spherical shape becomes more pronounced and the interaction with the substrate increases—effects not captured in this simple theoretical picture.

Cathodoluminescence (CL) was used to probe the local density of states of the nanocrystals, giving significant insight into the localization of the plasmon modes²⁴ (Figure 3). For both sizes shown, the truncated bipyramids and icosahedra exhibit a 3-fold symmetric dipole response (Figure 3b). This is consistent with our theoretical simulations, shown in Figure 3c, where we calculate the far-field emission produced by the nanocrystals when excited by a single dipole placed at different positions on a plane 5 nm above the nanocrystal (simulating the electron excitation beam). These simulations were obtained by solving Maxwell's equations using a finite difference time-domain numerical solver (Lumerical FDTD Solutions).

We also used scanning transmission electron microscopy (STEM) and electron energy-loss spectroscopy (EELS) to characterize the Al nanocrystal plasmon modes (Figure 4); such techniques allow the identification and mapping of resonances with high spatial resolution.²³ Strong plasmon resonances that were well-defined both spatially and spectrally were observed consistently in all single nanocrystals studied. STEM-EELS was performed on a monochromated, probe-corrected FEI Titan Themis operated at 200 kV and equipped with a Gatan Quantum ERS imaging filter; raw data from multiple beam positions are presented in Figure 4a. In the raw spectra, three main features can be observed: the tail of the zero-loss peak decaying in intensity with increasing energy (all spectra), the low-loss intensity (2–8 eV) due to LSPR interactions (surface positions) and the Al metal bulk plasmon at 14.9 eV (center of the particle). For the representative 166 nm diameter Al nanocrystal studied here, three prominent LSPR modes were found: the lowest energy at 3.3 eV and intermediate energy modes at 5.5 and 7.1 eV (Figure 4b). Plasmon maps (Figure 4c) were generated from plotting the contribution of each resonant mode at each pixel for the modes (Figure 4b) extracted from the STEM-EELS data cube with non-negative matrix functionalization (performed in HYPERSPY).^{25,27} These maps consistently display 3-fold symmetry, corroborating the CL results. The field intensity for the lowest energy dipolar 3.3 eV plasmon mode (Figure 4c, top) is strongly localized at the tips of the particle, similar to the lower energy modes of a nanocube.^{25,26} The 5.5 eV mode (Figure 4c, center) is a quadrupolar LSPR with field intensity localized at the faces of the structure; analogies can again be made with the face mode of a nanocube.²⁵ The 7.1 eV mode (Figure 4c, bottom) is also localized at the nanoparticle faces and is consistent with a higher order, octupolar plasmon mode.

STEM-EELS not only provides information on plasmon distribution, it can also characterize the elemental composition of the nanocrystal, through the oxygen-K (O–K) core-loss signal and Al bulk plasmon. Figure 4d shows core-loss EELS in the O–K region for multiple beam positions and the inset presents a map of the background-subtracted O–K intensity. The oxide layer fully surrounds the particle, albeit the O–K signal at the center of the particle is damped by multiple scattering (the thickness of the particle being 166 nm). The thin oxide layer does not prevent efficient plasmon excitation, either in optical spectroscopy or electron-based techniques.⁴ EELS also reveals the particularly pronounced bulk plasmon of Al (Figure 4a). This very strong mode, observed around 14.9 eV, confirms the nanoparticle composition.

These uniform, robust, and air-stable nanocrystals are likely to be useful in many of the applications currently being pursued with gold and silver nanoparticles, including chemical sensing, surface-enhanced spectroscopies, and plasmonic materials and devices. In addition, they provide a far more sustainable alternative to gold and silver nanoparticles currently in widespread use, making them attractive for large-scale or large-area applications not considered practical previously, such as smart windows or displays, even paints and coatings. These new materials may replace organic pigments in applications where conditions such as long-term UV exposure may prove limiting to material lifetimes.

■ ASSOCIATED CONTENT

📄 Supporting Information

XPS-depth profiling of the aluminum nanocrystal product. Histograms of Al NCs represented in Figure 1 and average diameters of particles synthesized with more THF volume fractions. TEM images of Al NCs washed in THF and IPA. EELS mapping of LSPR of another particle and intensity of EELS spectral components at various positions. This material is available free of charge via the Internet at <http://pubs.acs.org>.

■ AUTHOR INFORMATION

Corresponding Author

*E-mail: halas@rice.edu.

Funding

This work was supported by the Robert A. Welch Foundation under Grants C-1220 (N.J.H.), C-1222 (P.N.), and C-0976 (K.H.W.); the Air Force Office of Scientific Research (AFOSR) FA9550-15-1-0022, NSF MRI ECCS 1040478, the Army's in-house laboratory independent research program, and the Army Research Office MURI W911NF-12-0407. A.M. acknowledges financial support from the Welch foundation through the J. Evans Attwell-Welch Postdoctoral Fellowship Program of the Smalley Institute of Rice University (Grant L-C-004).

Notes

The authors declare no competing financial interest.

■ ACKNOWLEDGMENTS

The authors would like to thank Emrah Yücelen, Bob Y. Zheng, Amanda M. Goodman, Sandra W. Bishnoi, Desmond E. Schipper, and Felix Berg for productive discussions.

■ REFERENCES

- (1) Alayoglu, S.; Nilekar, A. U.; Mavrikakis, M.; Eichhorn, B. *Nat. Mater.* **2008**, *7*, 333–338.
- (2) Atwater, H. A.; Polman, A. *Nat. Mater.* **2010**, *9*, 205–213.
- (3) Hu, J.; Chen, L.; Lian, Z.; Cao, M.; Li, H.; Sun, W.; Tong, N. *J. Phys. Chem. C* **2012**, *116*, 15584–15590.
- (4) Knight, M. W.; King, N. S.; Liu, L.; Everitt, H. O.; Nordlander, P. *ACS Nano* **2014**, *8*, 834–840.
- (5) Knight, M. W.; Liu, L.; Wang, Y.; Brown, L.; Mukherjee, S.; King, N. S.; Everitt, H. O.; Nordlander, P.; Halas, N. J. *Nano Lett.* **2012**, *12*, 6000–6004.
- (6) Linic, S.; Christopher, P.; Ingram, D. B. *Nat. Mater.* **2011**, *10*, 911–921.
- (7) Schade, M.; Fuhrmann, B.; Bohley, C.; Schlenker, S.; Sardana, N.; Schilling, J.; Leipner, H. S. *J. Appl. Phys.* **2014**, *115*, 084309.
- (8) Eghtedari, M.; Oraevsky, A.; Copland, J. A.; Kotov, N. A.; Conjusteau, A.; Motamedi, M. *Nano Lett.* **2007**, *7*, 1914–1918.
- (9) Lohse, S. E.; Burrows, N. D.; Scarabelli, L.; Liz-marza, L. M.; Murphy, C. J. *Chem. Mater.* **2014**, *26*, 34–43.
- (10) Brien, M. N. O.; Jones, M. R.; Brown, K. A.; Mirkin, C. A. *J. Am. Chem. Soc.* **2014**, *136*, 7603–7606.
- (11) Chan, G. H.; Zhao, J.; Schatz, G. C.; Duyne, R. P. Van. *J. Phys. Chem. C* **2008**, *112*, 13958–13963.
- (12) Chung, S. W.; Gulians, G. A.; Bunker, C. E.; Hammerstroem, D. W.; Deng, Y.; Burgers, M. A.; Jelliss, P. A.; Buckner, S. W. *Langmuir* **2009**, *25*, 8883–8887.
- (13) Shahravan, A.; Desai, T. G.; Matsoukas, T. *ACS Appl. Mater. Interfaces* **2014**, *6*, 7942–7947.
- (14) Zidan, R. A.; Takara, S.; Hee, A. G.; Jensen, C. M. *J. Alloys Compd.* **1999**, *285*, 119–122.
- (15) Gavrilenko, V. V.; Chekulaeva, L. A.; Zakharkin, L. I.; Khimicheskaya, S. *Bull. Acad. Sci. USSR Div. Chem. Sci.* **1977**, *26*, 1131–1134.
- (16) Arora, N.; Jagirdar, B. R. *J. Mater. Chem.* **2012**, *22*, 9058.

- (17) Jouet, R. J.; Warren, A. D.; Rosenberg, D. M.; Bellitto, V. J.; Park, K.; Zachariah, M. R. *Chem. Mater.* **2005**, *17*, 2987–2996.
- (18) Lewis, W. K.; Rosenberger, A. T.; Gord, J. R.; Crouse, C. A.; Harruff, B. A.; Fernando, K. A. S.; Smith, M. J.; Phelps, D. K.; Spowart, J. E.; Gulians, E. A.; Bunker, C. E. *J. Phys. Chem. C* **2010**, *114*, 6377–6380.
- (19) Meziani, M. J.; Bunker, C. E.; Lu, F.; Li, H.; Wang, W.; Gulians, E. A.; Quinn, R. A.; Sun, Y.-P. *ACS Appl. Mater. Interfaces* **2009**, *1*, 703–709.
- (20) Fernando, K. A. S.; Smith, M. J.; Harruff, B. A.; Lewis, W. K.; Gulians, E. A.; Bunker, C. E. *J. Phys. Chem. C* **2009**, *113*, 500–503.
- (21) Frankcombe, T. J. *Chem. Rev.* **2012**, *112*, 2164–2178.
- (22) Chou, N. H.; Ke, X.; Schiffer, P.; Schaak, R. E. *J. Am. Chem. Soc.* **2008**, *130*, 8140–8141.
- (23) Nelayah, J.; Kociak, M.; Stéphan, O.; García de Abajo, F. J.; Tencé, M.; Henrard, L.; Taverna, D.; Pastoriza-Santos, I.; Liz-Marzán, L. M.; Colliex, C. *Nat. Phys.* **2007**, *3*, 348–353.
- (24) García de Abajo, F. J. *Rev. Mod. Phys.* **2010**, *82*, 209–275.
- (25) Nicoletti, O.; de la Peña, F.; Leary, R. K.; Holland, D. J.; Ducati, C.; Midgley, P. A. *Nature* **2013**, *502*, 80–84.
- (26) Ringe, E.; McMahon, J. M.; Sohn, K.; Cogley, C.; Xia, Y.; Huang, J.; Schatz, G. C.; Marks, L. D.; Van Duyne, R. P. *J. Phys. Chem. C* **2010**, *114*, 12511–12516.
- (27) Ringe, E.; Collins, S. M.; DeSantis, C. J.; Skrabalak, S. E.; Midgley, P. A. *Proc. SPIE* **2014**, 9278, 92780J.